View metadata, citation and similar papers at core.ac.uk

brought to you by CORE

provided by Edinburgh Research Explorer

THE UNIVERSITY of EDINBURGH

Edinburgh Research Explorer

Structurally Flexible and Solution Stable [Ln 4 TM 8 (OH) 8 (L) 8 (O 2 CR) 8 (MeOH) y](ClO 4) 4 : A Playground for Magnetic Refrigeration

Citation for published version:
Hooper, TN, Inglis, R, Lorusso, G, Ujma, J, Barran, PE, Uhrin, D, Schnack, J, Piligkos, S, Evangelisti, M & Brechin, EK 2016, 'Structurally Flexible and Solution Stable [Ln 4 TM 8 (OH) 8 (L) 8 (O 2 CR) 8 (MeOH) y](ClO 4) 4 : A Playground for Magnetic Refrigeration', *Inorganic Chemistry*. https://doi.org/10.1021/acs.inorgchem.6b01730

Digital Object Identifier (DOI):
10.1021/acs.inorgchem.6b01730

Link:
Link to publication record in Edinburgh Research Explorer

Document Version:
Peer reviewed version

Published In:
Inorganic Chemistry

OPEN ACCESS

The structurally flexible and solution stable $[Ln_4TM_8(OH)_8(L)_8(O_2CR)_8(MeOH)_y](ClO_4)_4$: a playground for magnetic refrigeration

Thomas N. Hooper,[†] Ross Inglis,[†] Giulia Lorusso,[‡] Jakub Ujma,[†] Perdita E. Barran,[†,∥] Dusan Uhrin,[†] Jürgen Schnack,[§] Stergios Piligkos,*[¶] Marco Evangelisti*[‡] and Euan K. Brechin*[†]

[†]EaStCHEM School of Chemistry, The University of Edinburgh, David Brewster Road, Edinburgh, EH9 3FJ, UK.

[∥]Current address: School of Chemistry, The University of Manchester, Oxford Road, Manchester, M13 9PL, UK.

[‡]Instituto de Ciencia de Materiales de Aragón, CSIC-Universidad de Zaragoza, 50009 Zaragoza, Spain.

[§]Universität Bielefeld, Fakultät für Physik, Postfach 100131, 33501 Bielefeld, Germany.

[¶]Department of Chemistry, University of Copenhagen, Universitetsparken 5, 2100 Copenhagen, Denmark.

ABSTRACT: The family of compounds of general formula $[Ln^{III}_4TM^{II}_8(OH)_8(L)_8(O_2CR)_8(MeOH)_y](ClO_4)_4$ {$[Gd_4Zn_8(OH)_8(hmp)_8(O_2C^iPr)_8](ClO_4)_4$ (**1a**); $[Y_4Zn_8(OH)_8(hmp)_8(O_2C^iPr)_8](ClO_4)_4$ (**1b**); $[Gd_4Cu_8(OH)_8(hmp)_8(O_2C^iPr)_8](ClO_4)_4$ (**2a**); $[Y_4Cu_8(OH)_8(hmp)_8(O_2C^iPr)_8](ClO_4)_4$ (**2b**); $[Gd_4Cu_8(OH)_8(hep)_8(O_2C^iPr)_8](ClO_4)_4$ (**3a**); $[Gd_4Cu_8(OH)_8(Hpdm)_8(O_2C^tBu)_8](ClO_4)_4$ (**4a**); $[Gd_4Cu_8(OH)_8(ea)_8(O_2CMe)_8](ClO_4)_4$ (**5a**); $[Gd_4Ni_8(OH)_8(hmp)_8(O_2CEt)_8(MeOH)_6](ClO_4)_4$ (**6a**); $[Y_4Ni_8(OH)_8(hmp)_8(O_2CEt)_8(MeOH)_6](ClO_4)_4$ (**6b**); $[Gd_4Co_8(OH)_8(hmp)_8(O_2CEt)_8(MeOH)_6](ClO_4)_4$ (**7a**); $[Y_4Co_8(OH)_8(hmp)_8(O_2CEt)_8(MeOH)_6](ClO_4)_4$ (**7b**)} can be formed very simply and in high yields from the reaction of $Ln(NO_3)_3{\cdot}6H_2O$ and $TM(ClO_4)_2{\cdot}6H_2O$ and the appropriate ligand blend in a mixture of CH_2Cl_2 and MeOH in the presence of a suitable base. Remarkably, almost all the constituent parts, namely the lanthanide (or rare earth) ions Ln^{III} (here Ln = Gd or Y), the transition metal ions TM^{II} (here TM = Zn, Cu, Ni, Co), the bridging ligand L (Hhmp = 2-(hydroxymethyl)pyridine; Hhep = 2-(hydroxyethyl)pyridine; H_2pdm = pyridine-2,6-dimethanol; Hea = 2-ethanolamine) and the carboxylates can be exchanged whilst maintaining the structural integrity of the molecule. NMR spectroscopy of diamagnetic complex **1b** reveals the complex to be fully intact in solution with all signals from the hydroxide, ligand L and the carboxylates equivalent on the NMR timescale, suggesting the complex possesses greater symmetry in solution than in the solid state. High resolution nano-ESI mass spectrometry on dichloromethane solutions of **2a** and **2b** show both complexes are present in two charge states with little fragmentation; the most intense peak in each spectrum corresponding to $[Ln_4Cu_8(OH)_8(hmp)_8(O_2C^iPr)_8](ClO_4)_2^{2+}$. This family of compounds offers an excellent playground for probing how the magnetocaloric effect evolves by introducing either antiferromagnetic or ferromagnetic interactions, or magnetic anisotropy, by substituting the non-magnetic Zn^{II} (**1a**) with Cu^{II} (**2a**), Ni^{II} (**6a**) or Co^{II} (**7a**), respectively. The largest magnetocaloric effect is found for the ferromagnetic complex **6a**, while the predominant antiferromagnetic interactions in **2a** yield an inverse magnetocaloric effect, *i.e.*, the temperature increases on lowering the applied field, under the proper experimental conditions. In spite of increasing the magnetic density by adding ions that bring in antiferromagnetic interactions (**2a**) or magnetic anisotropy (**7a**), the magnetocaloric effect is overall smaller in **2a** and **7a** than in **1a**, where only four Gd^{III} spins per molecule contribute to the magnetocaloric properties.

INTRODUCTION

Cryogenic magnetic refrigeration is a target application for molecules containing one or more paramagnetic metal ions, the latter are now often referred to as Molecular Nanomagnets (MNMs). MNMs can display an enhanced magnetocaloric effect (MCE).[1] Technologically this is important since MNMs can be exploited for cooling applications *via* adiabatic demagnetization.[2] Recent studies have clearly demonstrated that the MCE of MNMs, with a particular blend of physical characteristics, can be much larger than that found in commercially exploited materials.[3] The recipe[4] for making such molecules requires them to have a negligible anisotropy, which permits facile polarisation of the net molecular spin, leading to a large magnetic entropy change, and has resulted in the publication of a number of homo- and heterometallic species containing, for example, Gd^{III} and octahedral, high-spin Fe^{III} and Mn^{II}, amongst others.[5] The first molecular cluster studied was actually a heterometallic $[Cr^{III}_7Cd]$ wheel,[6] but its applicability was restricted by the low value of its spin ground state, $S = 3/2$. A major breakthrough was accomplished through the synthesis and study of highly symmetric molecules with large values of the spin ground state, the first being an $[Fe_{14}]$ hexacapped hexagonal prism with an $S = 25$ ground state,[7] the second a ferromagnetic $[Mn_{10}]$ supertetrahedron with $S = 22$,[8] and the third a $[Mn_{14}]$ disc.[9] These early successes

laid the groundwork and established the protocols for making molecular coolers, and have resulted in an explosion of interest in the area in the last few years.[5] In 2009 the first Gd^{III} containing molecular refrigerants were reported - a fumarate based Gd^{III} dimer[10] and a mixed Mn^{III}/Gd^{III} calixarene cage,[11] and since then almost all reported molecular coolers have contained this ion.[12]

The construction of heterometallic cluster compounds is a very attractive option since this offers an enormous degree of flexibility, both in terms of synthetic variables and potential structural targets. In particular, the 3*d*-4*f* combination proffers enormous scope in design, in the ability to tune the magnitude and sign of nearest neighbour magnetic exchange parameters, and for developing magneto-structural correlations. For example, it is well known that Gd^{III}-Cu^{II} interactions are almost always ferromagnetic,[13] and this was recently exploited in the synthesis of a $[Gd^{III}_4Cu^{II}_5]$ molecular cooler.[14] Herein we continue this strategy by reporting the syntheses, structures and magnetic properties of a family of complexes of general formula $[Ln^{III}_4TM^{II}_8(OH)_8(L)_8(O_2CR)_8(MeOH)_y][X]_4$ in which almost all the constituent parts, namely the Lanthanide (or rare earth) ions Ln^{III} (here Ln = Gd or Y), the transition metal ions TM^{II} (here TM = Zn, Cu, Ni, Co), the bridging ligand L (Hhmp = 2-(hydroxymethyl)pyridine; Hhep = 2-(hydroxyethyl)pyridine; H_2pdm = pyridine-2,6-dimethanol; Hea = ethanolamine; Scheme 1),[15] and the carboxylates can be exchanged, whilst maintaining the structural integrity of the metallic core. We have previously communicated the synthesis of three compounds of the family, namely **1a**, **2a** and **6a** based on the Hhmp pro-ligand.[5e]

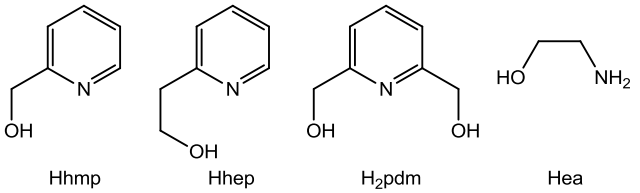

SCHEME 1. The pro-ligands employed in this work for the formation of polymetallic complexes. Hhmp = 2-(hydroxymethyl)pyridine; Hhep = 2-(hydroxyethyl)pyridine; H_2pdm = pyridine-2,6-dimethanol; Hea = 2-ethanolamine.

EXPERIMENTAL SECTION

All manipulations were performed under aerobic conditions using materials as received (reagent grade). Variable-temperature, solid state direct current (dc) magnetic susceptibility data down to 2 K were collected on a Quantum Design MPMS-XL SQUID magnetometer equipped with a 7 T dc magnet. Diamagnetic corrections were applied to the observed paramagnetic susceptibilities using Pascal's constants. Specific heat (*C*) measurements were carried out for temperatures down to 0.3 K by using a Quantum Design PPMS equipped with a ^{3}He cryostat. The experiments were performed on thin pressed pellets (*ca*. 1 mg) of polycrystalline samples, thermalized by *ca*. 0.2 mg of Apiezon N grease, whose contribution was subtracted by using a phenomenological expression.

X-ray Crystallography and Structure Solution

Diffraction data were collected between 100 and 150 K on a Bruker Smart Apex CCDC diffractometer, equipped with an Oxford Cryosystems LT device, using Mo radiation. See Table S1 and CIF files for full details. Complexes **1a**, **2a** and **6a** have been reported previously (CCDC 857983 - 857983) and the remaining complexes are reported here for the first time (CCDC 913278 - 913285).

NMR Spectroscopy

1D CSSF-NOESY spectra were acquired on an 800 MHz NMR spectrometer equipped with a TCI cryoprobe with z-gradients. The following parameters were used: acquisition and relaxation time of 2.4 and 1s, respectively; 8 scans were acquired in each of 10 increments of the chemical-shift-selective filter, which was optimised to yield zero excitation at the frequencies of the nearest protons (typically 27 to 83 Hz away). A 20 ms Gaussian pulse was used for the central spin-echo and the zero- and double-quantum coherences were suppressed *via* a 20 ms adiabatic pulse and a concomitant pulsed field gradient. NOE mixing times between 50 and 800 ms were used.

Mass Spectrometry

High resolution nano-ESI mass spectrometry was carried out on dichloromethane solutions of **2a** and **2b**. Borosilicate capillaries were used for nano-ESI, pulled in house with a P-97 Flaming/Brown Micropipette Puller. A user defined program adjusted the tip shape and orifice diameter of the capillaries for optimum ionisation. Voltage was applied to the solution *via* a platinum wire as described previously.[16] Mass Spectrometry analysis was perfomed on a Q-ToFII instrument that has been modified to facilitate the succesful transfer of intact non-covalent protein[17] and supramolecular complexes.[18]

Synthesis

Each member of the $[Ln_4TM_8(OH)_8(L)_8(O_2CR)_8(MeOH)_y](ClO_4)_4$ family was synthesised using a similar method. The lanthanide and transition metal salts, ligand L and sodium carboxylate were dissolved in stoichiometric amounts. A base was added to this stirred solution at room temperature, and after 30 minutes stirring the sample was filtered. X-ray quality single crystals were grown by slow evaporation of the filtrate or vapour diffusion of diethyl ether or *n*-hexane into samples of the filtrate. Full details are given below.

1a and **1b**: $Zn(ClO_4)_2{\cdot}6H_2O$ (0.372 g, 1.00 mmol), $Ln(NO_3)_3{\cdot}6H_2O$ (**1a**, Ln = Gd 0.226 g, 0.5 mmol; **1b**, Ln = Y, 0.192 g, 0.50 mmol) and NaO_2C^iPr (0.110 g, 1.00 mmol) were dissolved in a 50:50 mixture of CH_2Cl_2 and methanol (20 cm^3). 2-(hydroxymethyl)pyridine (Hhmp, 0.10 cm^3, 1.00 mmol) was added and after stirring for 5 minutes NaOMe (0.108 g, 2.00 mmol) was added and the mixture stirred for a further 20 minutes. The resulting solution was evaporated to dryness and re-dissolved in CH_2Cl_2 (15 cm^3) before being filtered to remove $NaNO_3$ and $NaClO_4$. Methanol (5 cm^3) was added to the filtrate and stirred. Vapour diffusion of diethyl ether into the solution yielded crystals after approximately 3 days.

1a Yield = 0.212 g, 51%. Anal. Calculated (found) for **1a**$\cdot 4H_2O$: $Zn_8Gd_4C_{80}H_{120}O_{52}N_8Cl_4$: C, 28.94 (29.29); H, 3.64 (3.32); N, 3.38 (3.56). **1b** Yield = 0.132 g, 35%. Anal.

Calculated (found) for **1b**·4H_2O: $Zn_8Y_4C_{80}H_{120}O_{52}N_8Cl_4$: C, 31.90 (32.44); H, 3.88 (3.68); N, 3.72 (3.98).

1b: ^{1}H NMR (800 MHz, 25 °C, CD_2Cl_2): δ = 8.80 (ddd, $^3J_{6,5}$ 5.4 Hz, $^4J_{6,4}$ 1.6 Hz 8H, H^6), 7.97 (ddd, $^3J_{4,3}$ 8.0 Hz, $^3J_{4,5}$ 7.5 Hz 8H, H^4), 7.48 (dd, 8H, H^5), 7.45 (d, 8H, H^3), 5.05 (d, $^2J_{1A,1B}$ 17.2 Hz, 8H, H^{1A}), 4.79 (d, 8H, H^{1B}), 4.35 (s, 8H, H^7), 1.58 (sept, , 8H, H^8), 0.88 (d, $^3J_{8,9}$ 7.0 Hz, 24H, H^9), 0.77 (d, $^3J_{8,10}$ 7.0 Hz, 24H, H^{10}). ^{13}C{^{1}H} NMR (100.6 MHz, 25 °C, CD_2Cl_2): δ = 187.1 (C^7), 161.0 (Ar) 147.7 (Ar), 140.5 (Ar), 123.8 (Ar), 122.2 (Ar), 63.6 (C^1), 36.5 (C^8), 19.6, 19.4 (C^{8,9}) ppm. See figure 7 for NMR numbering scheme.

2a and **2b**: $Cu(ClO_4)_2$·6H_2O (0.370 g, 1.0 mmol), $Ln(NO_3)_3$·6H_2O (**2a**, Ln = Gd 0.226 g, 0.5 mmol; **2b**, Ln = Y, 0.192 g, 0.5 mmol) and NaO_2C^iPr (0.110 g, 1.0 mmol) were dissolved in a 75:25 mixture of CH_2Cl_2 and methanol (20 cm^3). Hhmp (0.10 cm^3, 1.0 mmol) was added and after stirring for 5 minutes NaOMe (0.108 g, 2.0 mmol) was added and the mixture stirred for a further 20 minutes. The resulting solution was evaporated to dryness and re-dissolved in CH_2Cl_2 (15 cm^3) before being filtered to remove $NaNO_3$ and $NaClO_4$. Methanol (5 cm^3) was added to the filtrate and stirred. Slow evaporation of the filtrate yielded crystals after approximately 3 days.

2a Yield = 0.247 g, 61%. Anal. Calculated (found) for **2a**·0.5H_2O: $Cu_8Gd_4C_{80}H_{113}O_{48.5}N_8Cl_4$: C, 29.64 (29.86); H, 3.51 (3.36); N, 3.46 (3.26). **2b** Yield = 0.275 g, 74%. Anal. Calculated (found) for **2b**·0.5H_2O: $Cu_8Y_4C_{80}H_{113}O_{48.5}N_8Cl_4$: C, 32.35 (32.50); H, 3.84 (3.62); N, 3.78 (3.74).

3a: $Cu(ClO_4)_2$·6H_2O (0.370 g, 1.0 mmol), $Gd(NO_3)_3$·6H_2O (0.226 g, 0.5 mmol) and NaO_2C^iPr (0.110 g, 1.0 mmol) were dissolved in a 50:50 mixture of CH_2Cl_2 and methanol (20 cm^3). 2-(hydroxyethyl)pyridine (Hhep 0.11 cm^3, 1.0 mmol) was added and after stirring for 5 minutes NEt_3 (0.28 cm^3, 2.0 mmol) was added and the mixture stirred for a further 20 minutes. The reaction mixture was filtered and slow evaporation of the filtrate yielded crystals after approximately 5 days.

3a Yield = 0.083 g, 21%. Anal. Calculated (found) for **3a**·8MeOH: $Cu_8Gd_4C_{96}H_{160}O_{56}N_8Cl_4$: C, 32.00 (31.93); H, 4.48 (4.47); N, 3.11 (3.16).

4a: $Cu(ClO_4)_2$·6H_2O (0.370 g, 1.0 mmol), $Gd(NO_3)_3$·6H_2O (0.226 g, 0.5 mmol) and NaO_2C^tBu (0.124 g, 1.0 mmol) were dissolved in a 50:50 mixture of CH_2Cl_2 and methanol (20 cm^3). Pyridine-2,6-dimethanol (H_2pdm, 0.139 g, 1.0 mmol) was added and after stirring for 5 minutes NEt_3 (0.28 cm^3, 2.0 mmol) was added and the mixture stirred for a further 20 minutes. The reaction mixture was filtered and slow evaporation of the filtrate yielded crystals after approximately 7 days.

4a Yield = 0.064 g, 14%. Anal. Calculated (found) for **4a**·2MeOH·2H_2O: $Cu_8Gd_4C_{98}H_{148}O_{60}N_8Cl_4$: C, 31.99 (32.08); H, 4.06 (4.08); N, 3.05 (3.16).

5a: $Cu(ClO_4)_2$·6H_2O (0.370 g, 1.0 mmol), $Gd(NO_3)_3$·6H_2O (0.226 g, 0.5 mmol) and NaO_2CMe (0.082 g, 1.0 mmol) were dissolved in a 50:50 mixture of CH_2Cl_2 and methanol (20 cm^3). 2-ethanolamine (Hea, 1.0 cm^3, 1.0 mol dm^{-3} solution in MeOH, 1.0 mmol) was added and after stirring for 5 minutes NEt_3 (0.28 cm^3, 2.0 mmol) was added and the mixture stirred for a further 20 minutes. Vapour diffusion of diethyl ether into the solution yielded crystals after approximately 5 days.

5a Yield = 0.112 g, 34%. Anal. Calculated (found) for **5a**·2H_2O: $Cu_8Gd_4C_{32}H_{84}O_{50}N_8Cl_4$: C, 14.44 (14.15); H, 3.18 (2.86); N, 4.21 (4.08).

6a and **6b**: $Ni(ClO_4)_2$·6H_2O (0.366 g, 1.0 mmol), $Ln(NO_3)_3$·6H_2O (**6a**, Ln = Gd 0.226 g, 0.5 mmol; **6b**, Ln = Y, 0.192 g, 0.5 mmol) and NaO_2CEt (0.096 g, 1.0 mmol) were dissolved in a 50:50 mixture of CH_2Cl_2 and methanol (20 cm^3). Hhmp (0.10 cm^3, 1.0 mmol) was added and after stirring for 5 minutes NaOMe (0.108 g, 2.0 mmol) was added and the mixture stirred for a further 20 minutes. The resulting solution was evaporated to dryness and re-dissolved in a 50:50 mixture of CH_2Cl_2 and methanol (20 cm^3) before being filtered. Vapour diffusion of diethyl ether into the filtrate yielded crystals after approximately 14 days.

6a Yield = 0.087 g, 21%. Anal. Calculated (found) for **6a**·4H_2O: $Ni_8Gd_4C_{78}H_{128}O_{58}N_8Cl_4$: C, 28.00 (28.25); H, 3.86 (3.63); N, 3.35 (3.56). **6b** Yield = 0.102 g, 27%. Anal. Calculated (found) for **6b**·4H_2O: $Ni_8Y_4C_{78}H_{128}O_{58}N_8Cl_4$: C, 30.47 (30.38); H, 4.20 (4.11); N, 3.65 (3.71).

7a and **7b**: $Co(ClO_4)_2$·6H_2O (0.367 g, 1.0 mmol), $Ln(NO_3)_3$·6H_2O (**7a**, Ln = Gd 0.226 g, 0.5 mmol; **7b**, Ln = Y, 0.192 g, 0.5 mmol) and NaO_2CEt (0.096 g, 1.0 mmol) were dissolved in a 50:50 mixture of CH_2Cl_2 and methanol (20 cm^3). Hhmp (0.10 cm^3, 1.0 mmol) was added and after stirring for 5 minutes NaOMe (0.108 g, 2.0 mmol) was added and the mixture stirred for a further 20 minutes. The resulting solution was evaporated to dryness and re-dissolved in a 50:50 mixture of CH_2Cl_2 and methanol (20 cm^3) before being filtered. Vapour diffusion of diethyl ether into the filtrate yielded crystals after approximately 14 days.

7a Yield = 0.056 g, 13%. Anal. Calculated (found) for **7a**: $Co_8Gd_4C_{78}H_{120}O_{54}N_8Cl_4$: C, 28.58 (28.83); H, 3.69 (3.92); N, 3.42 (3.43). **7b** Yield = 0.035 g, 9%. Anal. Calculated (found) for **6b**: $Co_8Y_4C_{80}H_{128}O_{56}N_8Cl_4$: C, 31.18 (31.31); H, 4.03 (4.12); N, 3.73 (3.98).

RESULTS AND DISCUSSION

Structural Description

In each case the Gd^{III} and Y^{III} analogues of each of the compounds were found to be isostructural, with only very small differences in bond lengths and angles, and so for the sake of brevity we provide a generic structure description, highlighting any differences. The core of each molecule (Figure 1 shows complex **2a**) consists of a square (or wheel) of four corner-sharing $\{Ln^{III}_2TM^{II}_2O_4\}^{6+}$ cubanes. The shared corners are the Ln ions, which thus themselves form an inner $\{Ln^{III}_4\}$ square, each edge of which is occupied by two μ_3-OH$^-$ ions that further bridge to a TM^{II} ion. The μ_3-L$^-$ ions chelate the TM^{II} ions and use their O-arm to further bridge to the second TM^{II} ion in the same cubane and to one Ln^{III} ion. There are two carboxylates per cubane, each μ-bridging across a TM^{II}···Ln^{III} square face, alternately above and below the plane of the $\{Ln^{III}_4\}$ square. The latter is approximately 4 Å^2 with the TM^{II}···TM^{II} intracubane distance being ~3.2 Å. In **2a** the Cu^{II} ions are 5-coordinate and square pyramidal in geometry with the Jahn-Teller (JT) axis being the apex of the pyramid; the length of the Cu-O(apex) bond (average 2.290 Å) being at least 0.25 Å longer than

the equatorial bond lengths. The Gd^{III} ions are eight-coordinate and in square antiprismatic geometries.

Complexes **2a** and **2b** both crystallise in the tetragonal space group *P*4*nc* and pack (Figure 2) in layers of offset sheets with two disordered perchlorate counter ions sitting in the cavities above and below the $[Ln_4]$ plane, hydrogen bonded to the μ_3-OH^- ligands. The remaining two perchlorate anions fill voids between molecules. The Zn^{II} containing complexes $[Ln_4Zn_8(OH)_8(hmp)_8(O_2C^iPr)_8][ClO_4]_4$ (Ln = Gd, **1a**; Ln = Y, **1b**) are isostructural. Each Zn^{II} centre is five-coordinate, but unlike the Cu^{II} ions in **2a** and **2b**, is in a distorted trigonal bipyramidal geometry.

If the chelating ligand hmp^- in **2a** is replaced by hep^-, a similar molecular structure $[Gd_4Cu_8(OH)_8(hep)_8(O_2C^iPr)_8][ClO_4]_4$ (**3a**) is obtained (Figure 3). However, upon closer inspection subtle differences are evident. The complex crystallises in a lower symmetry space group (*C*2/*c*) with differences in the coordination of the Cu^{II} ions. In **2a** and **2b** the Cu^{II} ions are square-based pyramidal in geometry, but in **3a** the geometries are less well defined: Cu(1) remains square-base pyramidal with a significant JT distortion, but Cu(2) is closer to trigonal bipyramidal with a less pronounced JT axis. Cu(3) and Cu(4) show similar behaviour. Further analysis reveals the extra CH_2 group in the alkoxide arm of the hep^- ligand to be responsible for this change.

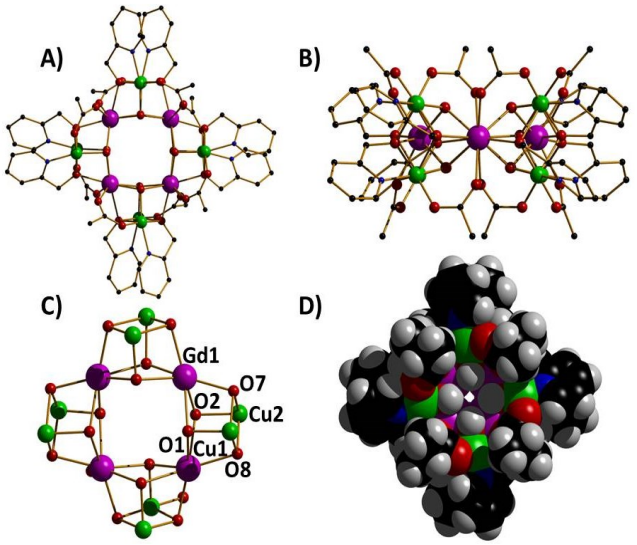

Figure 1. The molecular structure of the cation of complex **2a** viewed perpendicular (A) and parallel (B) to the $\{Gd_4\}$ plane. Gd = purple, Cu = green, O = red, N = blue, C = black. H atoms, some C atoms and the ClO_4^- anions are omitted for clarity. C) The metal–oxygen core, indicating the corner-sharing $\{Gd_2Cu_2O_4\}$ cubanes; Cu-O-Cu = 95.64–96.56°, Cu-O-Gd = 95.26–101.87°, Gd-O-Gd=110.90–111.88°. D) Space-filling representation of the cation of **2a**.

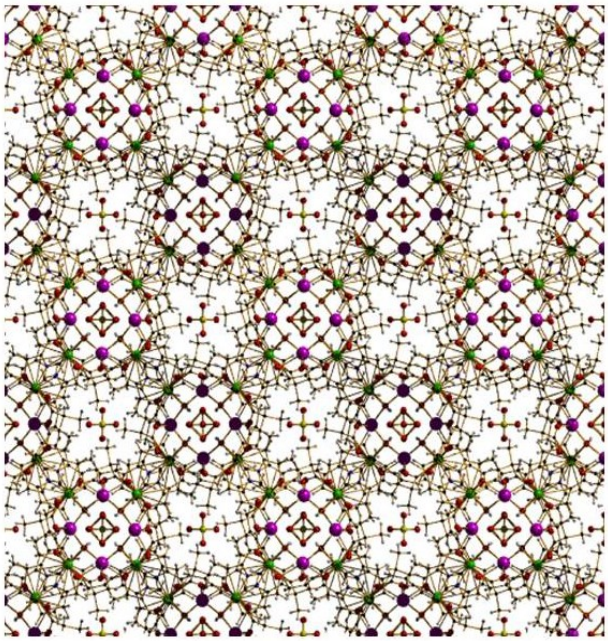

Figure 2. The packing of **2a** in the crystal, viewed down the *c*-axis.

The relative "flatness" of the coordinated hmp^- ligand in **2a** (Figure 3c) permits the two ligands in each cubane to pack together efficiently – *i.e.* the pyridyl rings are essentially parallel to one another (the mean planes create an angle of ~14° with respect to each other) – and this allows the Cu^{II} ions to possess square-pyramidal geometry. However, in **3a** sterics arising from the presence of the additional CH_2 group prevent such an orientation, and the ligands are rotated out of the plane; indeed, the two ligands are now essentially perpendicular to each other with the mean planes of the two pyridyl rings creating an angle of 83° with respect to each other (Figure 3D).

The chelating ligands, L, coordinate to the TM^{II} centre *via* a neutral N-donor and a μ_3-alkoxide arm with a 2 or 3 carbon chain in between, and it appears that any analogous ligand can be employed without significant alteration to the metallic core of the complex. Thus, use of H_2pdm (Scheme 1) affords $[Gd_4Cu_8(OH)_8(Hpdm)_8(O_2C^tBu)_8][ClO_4]_4$ (**4a**) and the use of Hea affords $[Gd_4Cu_8(OH)_8(ea)_8(O_2CMe)_8][ClO_4]_4$ (**5a**), with both structures being analogous to **2a**. In **4a** one of the arms per ligand L is unbound, with the pendant alcohol H-bonded to the MeOH of crystallisation and the ClO_4^- counter ions. The same is true of the carboxylate ligands (*i.e.* any carboxylate will work), and here of course the choice is essentially unlimited. Such flexibility in structure design is highly unusual in the chemistry of large polymetallic cage complexes – especially so given their solution stability, *vide infra* – and allows the chemist enormous scope for design and manipulation. For example, the ease with which the whole of the peripheral organic sheath can be changed can be exploited for surface deposition and analysis.[19] A sizeable change in relative molecular mass can also be achieved very simply; using 2-ethanolamine as the chelating ligand and replacing

the larger carboxylate ligands with acetate produces complex **5a** with a molecular mass more than 600 amu less than that complex **2a**. The magnetic density of a sample being an important ingredient in the recipe for constructing molecule-based cryocoolers.[3,4]

Moving along the first transition series to Ni^{II} yields $[Ln_4Ni_8(OH)_8(hmp)_8(O_2CEt)_8(MeOH)_6][ClO_4]_4$ (Ln = Gd, **6a**; Ln = Y, **6b**), and these complexes display notable differences to the Zn^{II} and Cu^{II} compounds (Figure 4 shows **6a**). The Ni^{II} ions are 6-coordinate and in distorted octahedral geometries. Their coordination spheres contain the same five donors found in **1-5** plus (in total) six terminally bonded methanol molecules and two extra donor atoms from a change in coordination mode of the carboxylate ligand. Each Ni^{II} centre is at the corner of one cubane, so four of the donor ligands remain the same. Ni(1) is further coordinated by one μ-bridging carboxylate (across the Gd1···Ni1 face of the cube) and one methanol solvent molecule. Ni(2) is ligated by a methanol molecule and one carboxylate which has switched to a [syn, syn, anti] μ_3-bridging mode (Figure 4); *i.e.* the μ_3-carboxylate bridges across the Ln(2)···Ni(4) face in the usual syn, syn fashion, with O(9) further bridging to Ni(2). Ni(3) has coordination from two syn, syn μ-bridging carboxylates and Ni(4) is coordinated by one methanol molecule and O(10) from the μ_3-carboxylate. This change in coordination mode means that overall the carboxylate ligands have lost the regular up/down alternating pattern found in compounds **1-5**. The Co^{II} complexes $[Ln_4Co_8(OH)_8(hmp)_8(O_2CEt)_8(MeOH)_6][ClO_4]_4$ (Ln = Gd, **7a**; Ln = Y, **7b**) are isostructural to their Ni^{II} congeners (Figure 5 shows complex **7a**).

A search of the literature reveals the most structurally similar compound to those reported herein to be the complex $[Ln^{III}_4Cu^{II}_8L_8(H_2O)(OH)_8Cl_{10}(H_2O)_4]Cl_2\cdot 6MeCN$ (HL = 5,7-di-*t*-butyl-2-methylenehydroxylbenzoxazole) reported by Luneau *et al.*[20] The metallic core of linked cubanes in the latter has similar connectivity but is highly distorted and also features an unusual μ-bridging H_2O at the centre of a $[Ln_4]$ rhombus. The corner sharing $[Ln^{III}_2TM^{II}_2O_4]^{6+}$ cubane motif is also found in the complex $[Dy^{III}_3Cu^{II}_6L_6(OH)_6(H_2O)_{10}]Cl_2\cdot ClO_4$ (LH_2=1,1,1-trifluoro-7-hydroxy-4-methyl-5-azahept-3-en-2-one) which has three linked cubanes affording a central $[Ln_3]$ triangle,[21] and two similar examples of four corner-sharing partial $[Ln^{III}_2TM^{III}O_4]^{5+}$ cubanes are found in the calix[n]arene-based complex $[Mn^{III}_4Ln^{III}_4(OH)_4(C[4])_4(NO_3)_2(H_2O)_6](OH)_2$ (C[4] = calix[4]arene)[22] and the diol-based species $[Mn^{III}_4Ln^{III}_4(OH)_4(N_3)_4(O_2C^tBu)_8(t\text{-bdea})_4]$ (*t*-bdea = *t*-butyldiethanolamine).[23] Examples of other $[Ln^{III}_4TM^{II}_8]$ complexes which have been reported in the literature include the complexes $[Gd^{III}_4Co^{II}_8(OH)_4(NO_3)_4(O_3P^tBu)_8(O_2C^tBu)_{16}]$ and $[Gd^{III}_4Co^{II}_8(O_3P^tBu)_6(O_2C^tBu)_{16}]$, but the metallic cores of these structures are significantly different from those reported here.[24]

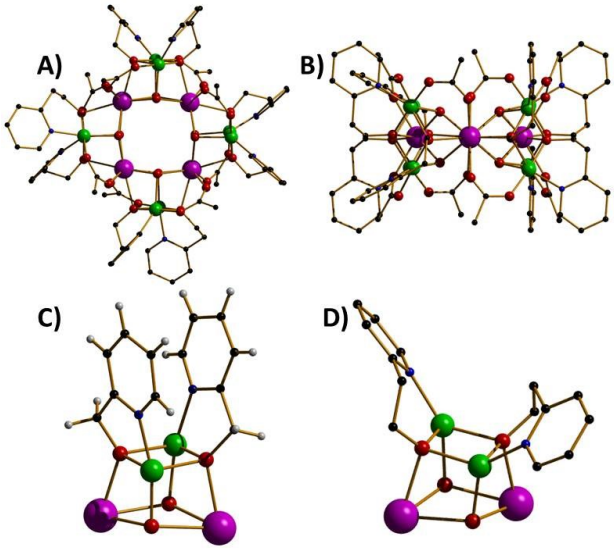

Figure 3. The molecular structure of the cation of complex **3a** viewed perpendicular (A) and parallel (B) to the $\{Gd_4\}$ plane. Gd = purple, Cu = green, O = red, N = blue, C = black. H atoms, some C atoms and the ClO_4^- anions are omitted for clarity. Comparison of the cubane moieties from compounds **2a** (C) and **3a** (D) highlighting difference in ligand geometry and coordination at the Cu^{II} centres.

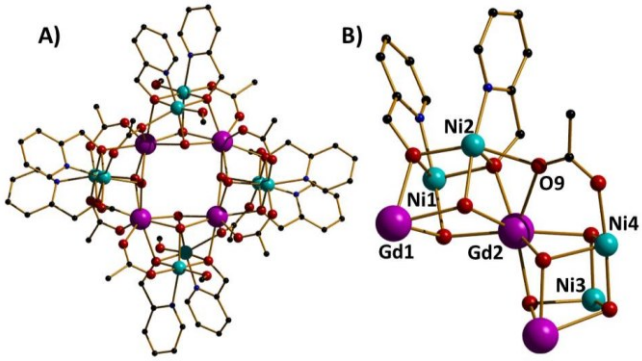

Figure 4. The molecular structure of the cation of **6a** viewed perpendicular to the $\{Gd_4\}$ plane (A). Close-up of two corner sharing $[Gd_2Cu_2]$ cubanes highlighting the syn, syn, anti-bridging mode of the μ_3-carboxylate (B). H atoms, some C atoms and the ClO_4^- anions are omitted for clarity. Gd = purple, Ni = light blue, C = black, O = red, N = blue.

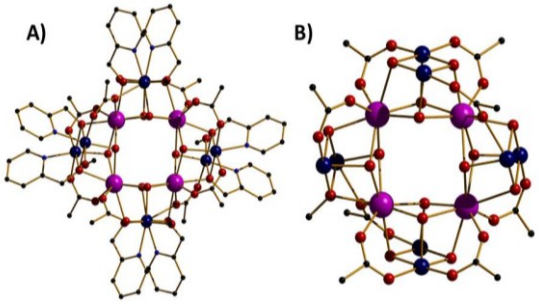

Figure 5. The molecular structure of the cation of **7a** (A) viewed perpendicular to the $\{Gd_4\}$ plane. The central core of **7a** highlighting the two distinct bridging modes of the carboxylate ligands (B). Gd = purple, Co = dark blue, C = black, O = red, N = blue.

Solution NMR Spectroscopy

Diamagnetic complex **1b** was studied in solution using ^{1}H NMR spectroscopy at 800 MHz. Dissolved in a non-coordinating solvent (d_2-dichloromethane), the complex appears to be fully intact, showing one set of ^{1}H resonances (Fig. 6) for each of the hydroxide, hmp$^-$ and carboxylate ligands. This indicates that the complex possesses greater symmetry in solution than in the solid state. The ^{1}H NMR spectrum shows two protons of the CH_2 group of the hmp$^-$ ligands to be non-equivalent. Equally, the two methyl groups on the carboxylate ligand ($^-O_2CCHMe_2$) are chemically non-equivalent and show separate signals. This is indicative of restricted rotation which occurs when the ligands are bound in a complex causing a loss of symmetry. Similarly, the ^{13}C NMR spectrum of **1b** shows two distinct resonances in the methyl region, confirming the non-equivalence of the carboxylate methyl groups.

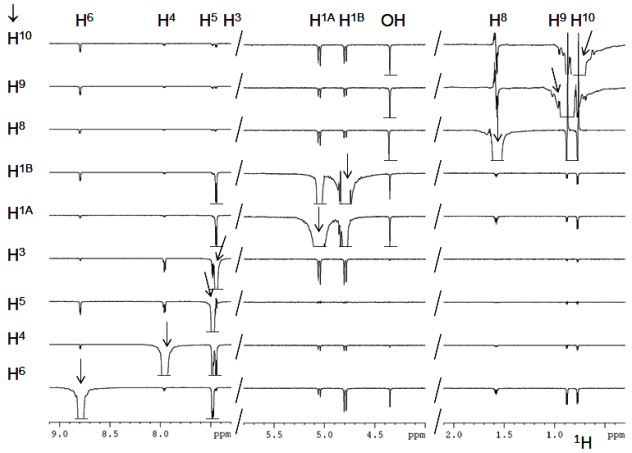

Figure 6. 800 MHz 400 ms mixing time 1D CSSF-NOESY spectra of **1b**. Arrows indicate the selectively inverted proton resonance. Horizontal dotted lines indicate cut-off levels of signals. Spectra are presented as three separate regions.

The ^{1}H NMR spectrum showed no significant changes when the sample was cooled to –60 °C, indicating that the dynamic processes that are responsible for time averaging of chemical environments of protons and carbons are too fast on the NMR timescale under these conditions. Nuclear Overhauser Spectroscopy (NOESY) confirmed that the complex is intact, as proton-proton NOEs were observed between the hmp$^-$ and carboxylate groups of ligands. In addition, these NOEs were negative, which is consistent with the large molecular weight of the complex. With the exception of an NOE between the two CH_2 protons (~14 %), the observed NOEs were generally very small, some as little as 0.01%. This is a consequence of the large inter proton distances (3.5 – 7.0 Å) in **1b** and the internal dynamics, which causes the chemical shift averaging discussed above. Such small NOEs are difficult to observe, nevertheless their presence can be established using NOE experiments involving pulsed field gradients.[25-27] The consistency of the observed NOEs was confirmed by recording spectra with different NOE mixing times (50 – 800 ms). As expected for true NOE peaks, the signal intensity of each proton increased steadily with increasing mixing time. (Fig. S1, supporting information). At the same time, the relative intensities of individual proton pairs did not change with increasing mixing time, indicating that spin-diffusion effects can be neglected. NOEs observed in the 400 ms mixing time spectra, which were largely free of *J* cross-talks, were quantified (Table S2). Analysis of this NOE data yielded interesting and self-consistent results, which are discussed next.

We start with the analysis of the aromatic protons. While the NOEs between H^3 or H^4, and both H^{1A} and H^{1B} protons are practically identical, the H^6 - H^{1B} NOE is 3.5-times more intense than the H^6-H^{1A} NOE. The same relative ratio was found for the H^{1B}-H^6 and H^{1A}-H^6 NOEs. Considering one hmp$^-$ ligand, the H^6- $H^{1A,1B}$ distance is larger than the H^4-$H^{1A,1B}$ distance, nevertheless the H^6-H^{1B} NOE is 4-fold bigger than the H^4-H^{1B} NOE. These observations indicate that NOEs involving H^3 or H^4 and H^{1A} or H^{1B} are between protons of the same hmp$^-$ ligand, while the H^6-H^{1B} NOE is between the protons of the two neighbouring hmp$^-$ ligands attached to the same cubane. At the same time, H^6 is closer to H^{1B} than H^{1A} of the other hmp$^-$ ligand (Fig. 7). Proton H^5 shows NOEs only to H^4 and H^6, which indicates that it points away from any aliphatic protons.

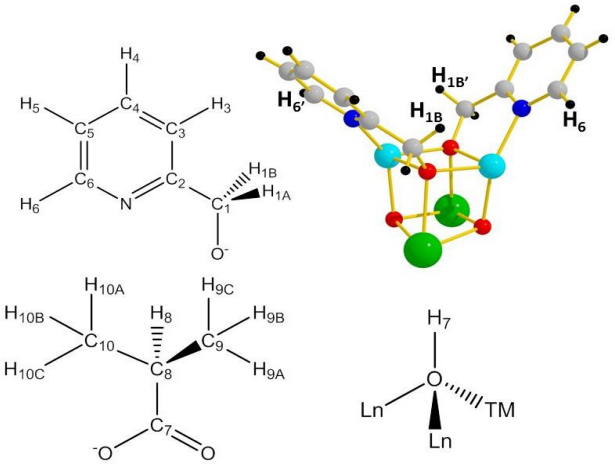

Figure 7. Numbering scheme of the ligands and part of the molecular structure of **1b** showing the hmp$^-$ ligand orientation in the cubane. Y green, Zn pale blue, C grey, O red, N blue, H black.

The CH_3 protons resonating at 0.77 ppm have NOEs to H^{1A} and H^{1B} protons which are twice the size of those observed from the CH_3 protons resonating at 0.88 ppm (Table S2). Analysis of the X-ray structure shows that the H^{1A}-H^{10} and H^{1B}-H^{10} distances are on average 1 Å shorter than the H^{1A}-H^9 and H^{1B}-H^9 distances. The CH_3 protons resonating at 0.77 and 0.88 ppm were therefore assigned to H^{10} and H^9, respectively. This is consistent with the C^9 methyl groups orientated more towards the centre of the molecule, while C^{10} is situated more towards the periphery. This assignment is further supported by the fact that H^9 shows a stronger NOE to $^-$OH than the H^{10} protons. The hydroxide protons show the most intense NOEs with H^{1A}, H^{1B} and H^8 protons, which reflects the shorter distances between the $^-$OH and

the aliphatic protons, than those between the -OH and the aromatic protons in the structure of **1b**. Finally, the shorter average H^8 - H^{1A} (4.4 Å) or H^8 - H^6 (4.5 Å) distances are reflected in more intense NOEs between these protons than observed between H^8 and H^{1B}, which are on average 5.0 Å apart. In summary, the solution structure reflects the basic features of the solid-state structure as illustrated by the analysis of ^{1}H-^{1}H nuclear Overhauser effects.

Mass Spectrometry

High resolution nano-ESI mass spectrometry was carried out on dichloromethane solutions of **2a** and **2b** and the results show both complexes are present in two charge states with little fragmentation (Figures 8-9). The most intense peak in each spectrum corresponds to $[Ln_4Cu_8(OH)_8(hmp)_8(O_2C^iPr)_8][ClO_4]_2^{2+}$ (Ln = Gd, **2a**; Ln = Y **2b**) and appears around m/z = 1516 for **2a** and m/z = 1379 for **2b**. The intact 4+ cationic complex remains associated to two of the perchlorate counter ions, likely those hydrogen bonded to the μ_3-OH groups, forming a dicationic charge state, which fits well with modelled data. A much less intense peak is observed in each spectrum at 3132 for **2a** and 2859 for **2b** which corresponds to the monocationic charge state of $[Ln_4Cu_8(OH)_8(hmp)_8(O_2C^iPr)_8][ClO_4]_3^{+}$ (Ln = Gd, 2a; Ln = Y **2b**) where three perchlorate anions are associated to the intact complex. The fact that this peak is much smaller suggests the third counter ion is weakly bound and this is consistent with the solid state observations with two perchlorate anions hydrogen bonded to hydroxide groups, while the remaining two show little evidence of strong interaction with the complex. That little fragmentation is observed suggests the complexes are stable in solution, in agreement with the NMR spectroscopy carried out on sample **1b**.

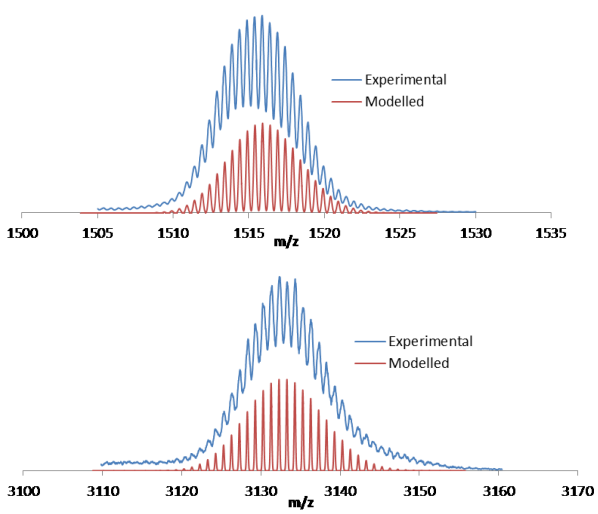

Figure 8. Experimental and modelled peaks from nESI mass spectrum of **2a** in CH_2Cl_2 showing $[Gd_4Cu_8(OH)_8(hmp)_8(O_2C^iPr)_8][ClO_4]_2^{2+}$ (top) and $[Gd_4Cu_8(OH)_8(hmp)_8(O_2C^iPr)_8][ClO_4]_3^{+}$ (bottom).

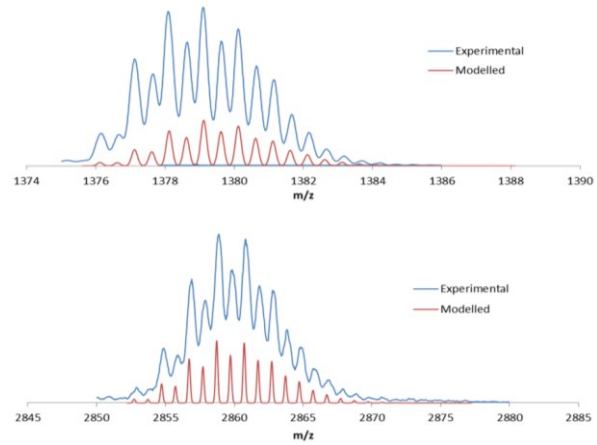

Figure 9. Experimental and modelled peaks from nESI mass spectrum of **2b** in CH_2Cl_2 showing $[Y_4Cu_8(OH)_8(hmp)_8(O_2C^iPr)_8][ClO_4]_2^{2+}$ (top) and $[Y_4Cu_8(OH)_8(hmp)_8(O_2C^iPr)_8][ClO_4]_3^{+}$ (bottom).

Magnetometry

To determine the dc molar magnetic susceptibility, χ_M, of complexes **1a**, **2a**, **2b**, **3a**, **4a**, **5a**, **6a**, **6b**, **7a** and **7b**, the magnetic moment, M, of polycrystaline powder samples of these complexes was measured in the applied field B = 0.1 T, over the 5 to 275 K temperature range. The experimental results for complexes **1a**, **2a**, **2b**, **6a**, **6b**, **7a** and **7b**, are shown in Figure 10 (panel a) in the form of $\chi_M T$ products, where $\chi = M/B$. Because of the similarity of the magnetic properties of complexes **3a**, **4a** and **5a** to the magnetic properties of complex **2a**, the experimental data for these complexes are shown in the SI (Fig S2-S3).

We first discuss the magnetic properties of the complexes containing Ln = Y^{III}. Since Y^{III} is a diamagnetic ion, in a first approximation we can consider that in complexes **2b**, **6b** and **7b**, the divalent transition-metal ions, TM^{II} in each of the four corner-sharing $\{Ln^{III}_2TM^{II}_2O_4\}^{6+}$ cubanes magnetically interact only with the other transition-metal ion located in the same $\{Ln^{III}_2TM^{II}_2O_4\}^{6+}$ cubane unit. Thus, within this model, the magnetic properties of complexes **2b**, **6b** and **7b**, can be considered as the simple superposition of the magnetic properties of four dimeric transition metal units. In addition, we consider all TM^{II} centres (and similarly in later sections, all Ln^{III} centres) within a given complex to be equivalent. Thus we use spin-Hamiltonian (1) to model the magnetic properties of complexes **2b**, **6b** and **7b**:

$$\hat{H} = 8\mu_B g_M B_0 \hat{S}_M + 4J_{MM'}\hat{S}_M \cdot \hat{S}_{M'} + 8D_M[\hat{S}^2_{z,M} - S_M(S_M+1)/3] \quad (1)$$

where M and M' refer to the two TM^{II} centres of a $\{Ln^{III}_2TM^{II}_2O_4\}^{6+}$ cubane, μ_B is the Bohr magneton, g is the g-factor of centre TM, $\hat{S}$ is a single-ion spin operator, J is the relevant isotropic exchange interaction parameter, D is the parameter of single-ion anisotropy axes, which are assumed to be uniaxial, and S is the total single-ion spin. In the case of **2b** the $\chi_M T$ product has a value of 3.47 cm^3 K mol^{-1} at 275 K. This corresponds to the spin-only value expected with g_{Cu} = 2.15. Thus, based on the experimental value of the $\chi_M T$ product at 275 K, we fix the g-value of Cu^{II} to g_{Cu} = 2.15 and we consider it isotropic because these thermodynamic measurements on polycrystalline powders do

not allow us to discern g-value anisotropy. The $\chi_M T$ product remains essentially constant in the 275 to 40 K temperature range, before decreasing at lower temperatures to reach a value of 1.6 cm^3 K mol^{-1} at 5 K. This behavior is indicative of the presence of weak antiferromagnetic interactions. For **2b**, the temperature dependence of the $\chi_M T$ product can be numerically fitted by full matrix diagonalisation of the 4×4 matrix representation of spin-Hamiltonian (1), by use of the simplex algorithm,[28] to give the best-fit parameter J_{CuCu} = 4.83 cm^{-1}. In the case of the Cu^{II} centre, D_{Cu} = 0 cm^{-1}, since S_{Cu} = 1/2. In addition, for all studied compounds we measured the variable-temperature-variable-field (VTVB) magnetic moment in the temperature range 2 to 7 K, and in magnetic fields of 0.5, 1.0, 2.0, 3.0, 4.0, 5.0, 6.0 and 7.0 Tesla. For **2b**, the results are shown in Figure 10 (panel b). The VTVB data of **2b** were independently fitted to spin-Hamiltonian (1) to yield a best-fit parameter J_{CuCu} = 4.83 cm^{-1}. The best-fit J_{CuCu} parameters resulting from two independent fits of data obtained in different temperature and field ranges are essentially identical and we can conclude that the determined J_{CuCu} parameter is accurate. Thus, the ground spin-state within each of the four corner-sharing $\{Y^{III}_2Cu^{II}_2O_4\}^{6+}$ cubanes is a spin-singlet (S = 0) separated from the unique excited state, which is a spin-triplet (S = 1), by J_{CuCu} cm^{-1}.

The $\chi_M T$ product of **6b** (panel a, Figure 10) has a value of 8.13 cm^3 K mol^{-1} at 275 K. This corresponds well to the spin-only value of 8.00 cm^3 K mol^{-1} expected for **6b** with g_{Ni} = 2.00. Thus we fix the g-value of Ni^{II} to g_{Ni} = 2.00. On lowering the temperature, the $\chi_M T$ product increases steadily to reach a maximum value of approximately 11.5 cm^3 K mol^{-1} at 20 K. On further lowering the temperature it decreases to reach a value of 9.3 cm^3 K mol^{-1} at 5 K. This behaviour is indicative of the presence of ferromagnetic interactions operating in **6b**. The temperature dependence of the $\chi_M T$ product can be numerically fitted to spin-Hamiltonian (1) by full matrix diagonalisation of the 9×9 matrix representation of spin-Hamiltonian (1) in a fashion analogous to **2b**. A satisfactory fit to the experimental $\chi_M T$ data can only be obtained by inclusion of a non-vanishing D_{Ni} parameter but its sign cannot be determined by these essentially high temperature data. The best-fit parameters obtained are J_{NiNi} = −21.68 cm^{-1} and D_{Ni} = −7.62 cm^{-1} or D_{Ni} = +7.12 cm^{-1}. To test the validity of the deduced parameters for **6b**, the VTVB data (panel c, Figure 10) were also fitted to spin-Hamiltonian (1). The J_{NiNi} parameter was fixed to the value obtained by fitting the $\chi_M T$ product, leaving D_{Ni} as the only free parameter. The best-fit D_{Ni} parameters in this case were D_{Ni} = −7.10 cm^{-1} or D_{Ni} = +11.77 cm^{-1}. However, as for the fit of the $\chi_M T$ product, fitting of the VTVB magnetic moment data does not lead to the determination of the sign of D_{Ni} even at these low temperatures. To unambiguously determine the sign and magnitude of D_{Ni}, low temperature Electron Paramagnetic Resonance (EPR) measurements will be necessary; these will be undertaken at a later date. In the case of **6b**, the ground spin-state within each of the four corner-sharing $\{Y^{III}_2Ni^{II}_2O_4\}^{6+}$ cubanes is a spin-quintet (S = 2) separated from the first excited state (a spin-triplet, S = 1), by $2J_{NiNi}$ cm^{-1} and from the second excited state (a spin-singlet, S = 0), by $3J_{NiNi}$ cm^{-1}.

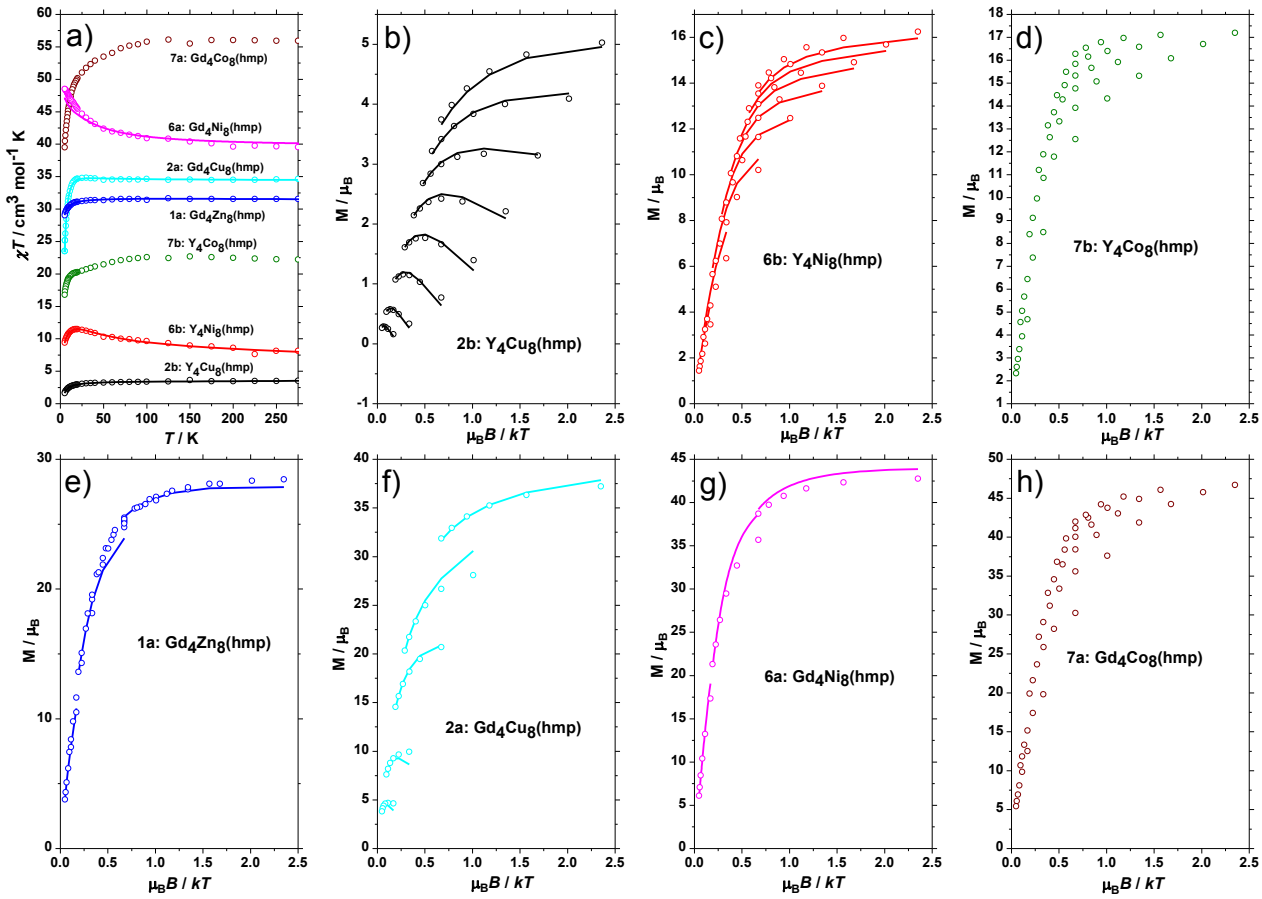

Figure 10. (a) Molar magnetic susceptibility ($\chi_M T$) versus T under a 0.1 T dc field plot. Molar magnetisation (M) as a function of applied magnetic field (B) at various temperatures (b-h). The solid lines are fits of the experimental data. See text for details.

The $\chi_M T$ product of **7b** (panel a, Figure 10) has a value of 22.20 cm^3 K mol^{-1} at 275 K. This corresponds to the spin-only value expected for **7b** assuming g_{Co} = 2.43. On lowering the temperature, the $\chi_M T$ product increases slightly to reach a maximum value of approximately 22.7 cm^3 K mol^{-1} at 150 K. On further lowering the temperature the $\chi_M T$ product decreases to reach a plateau of 20.28 cm^3 K mol^{-1} at 20 K before further decreasing to reach 16.76 cm^3 K mol^{-1} at 5 K. The VTVB data of **7b** are shown in Figure 10d. We have not attempted to model either, since the presence of the orbitally degenerate octahedral Co^{II} ion (possessing a $^4T_1$ ground term in O_h symmetry) renders the spin-Hamiltonian formalism inapplicable. Qualitatively, it seems that the Co^{II} ions interact antiferromagnetically. The appearance of two energy scales in the $\chi_M T$ product (150 K and 20 K) suggests that the unknown Hamiltonian is dominated by two energy scales representing the (possibly dominating) anisotropy as well as the exchange.

We now turn our attention to the Gd^{III} containing complexes, namely **1a**, **2a**, **6a**, and **7a**. We use the general form of isotropic spin-Hamiltonian (2) to interpret the magnetic properties of **1a**, **2a** and **6a**: where the index i runs through all twelve centres of **2a** and **6a** (Gd^{III} ions correspond to indices 1 to 4) and only through the Gd^{III} ions for **1a**, and g = 2 is the isotropic g-factor. For the interpretation of the magnetic properties of **1a**, only the first two terms of spin-Hamiltonian (2) are relevant. Due to the presence of Ni^{II} and Co^{II} ions in **6a** and **7a**, respectively, spin-Hamiltonian (2) must be modified in order to take into account the anisotropic contributions from these ions. These single-ion anisotropy terms destroy the spin rotational symmetry of (2), which together with the enormous dimension of the Hilbert space [1,048,576 and 268,435,456 for **6a** and **7a**, respectively] renders an exact treatment of **6a** demanding and of **7a** impossible. Thus, we neglect such terms in spin-Hamiltonian (2).

$$\begin{aligned}\hat{H} = g\mu_B B_0 \sum_i \hat{S}_i &+ J_{\mathrm{GdGd}}\left(\hat{S}_1\hat{S}_2 + \hat{S}_2\hat{S}_3 + \hat{S}_3\hat{S}_4 + \hat{S}_4\hat{S}_1\right) \\ &+ J_{\mathrm{MM'}}\left(\hat{S}_5\hat{S}_6 + \hat{S}_7\hat{S}_8 + \hat{S}_9\hat{S}_{10} + \hat{S}_{11}\hat{S}_{12}\right) \\ &+ J_{\mathrm{GdM}}\left[\begin{array}{l}\hat{S}_1\left(\hat{S}_5 + \hat{S}_6 + \hat{S}_{11} + \hat{S}_{12}\right) + \hat{S}_2\left(\hat{S}_5 + \hat{S}_6 + \hat{S}_7 + \hat{S}_8\right) + \\ \hat{S}_3\left(\hat{S}_7 + \hat{S}_8 + \hat{S}_9 + \hat{S}_{10}\right) + \hat{S}_4\left(\hat{S}_9 + \hat{S}_{10} + \hat{S}_{11} + \hat{S}_{12}\right)\end{array}\right]\end{aligned} \quad (2)$$

The $\chi_M T$ product of **1a** has a value of 31.5 cm^3 K mol^{-1} (Figure 10a) at 275 K, which is that expected from spin-only contributions to the magnetism, with g_{Gd} = 2. The temperature dependence of the $\chi_M T$ product of **1a** indicates the absence of sizeable exchange interactions between the Gd^{III} ions. The matrix representation of spin-Hamiltonian (2) for **1a** is of dimension 4,096×4,096 and can be diagonalised by

standard full matrix approaches. The $\chi_M T$ data can be numerically fitted to spin-Hamiltonian (2) to yield J_{GdGd} = 0.02 cm^{-1}. A single-point calculation of the VTVB magnetic moment data of **1a**, using the best-fit J_{GdGd} parameter from fitting of the $\chi_M T$ data, results in good agreement with the experimental data (Figure 10e). With these parameters the ground spin-state of **1a** is a S = 0 state, with numerous low-lying excited states.

The $\chi_M T$ product of **2a** has a value of 34.5 cm^3 K mol^{-1} (Figure 10a) at 275 K, which is a little lower than the 35.0 cm^3 K mol^{-1} expected from spin-only contributions to the magnetism with g_{Gd} = 2.00 and g_{Cu} = 2.15. The temperature dependence of the $\chi_M T$ product indicates the presence of antiferromagnetic interactions. The matrix representation of spin-Hamiltonian (2) for **2a** is of dimension 1,048,576 × 1,048,576 and cannot be diagonalised by use of standard numerical techniques as for all previously described complexes. We therefore employed home written software (ITO-MAGFIT[28]) that makes use of Irreducible Tensor Operator algebra[29] to block-diagonalise the spin-Hamiltonian. ITO-MAGFIT is a magnetisation fitting program that uses the Levenberg–Marquardt algorithm.[28] Calculation of the magnetic moment by block-diagonalisation of the spin-Hamiltonian matrix is greatly simplified if an isotropic g-value is employed since projection of the single-ion g-values to each individual total-spin state S can be avoided. This is the reason we use a unique isotropic g-value (g = 2) in spin-Hamiltonian (2) for modelling the magnetic properties of **2a**, even though we have previously deduced that g_{Cu} = 2.15 in **2b**. The best fit exchange parameters determined in this way for **2a** are J_{CuCu} = 11.84 cm^{-1}, J_{GdCu} = –1.38 cm^{-1} and J_{GdGd} = 0.20 cm^{-1}. These parameters are larger than those determined previously in **2b** (J_{CuCu} = 4.83 cm^{-1}) and **1a** (J_{GdGd} = 0.02 cm^{-1}), respectively. This may be due to the parameters being non-transferable between the complexes (*i.e.* the J values in different complexes are actually different), or may simply demonstrate the limit of our models. However, a single-point calculation of the VTVB magnetic moment data of **2a**, using the best-fit parameters from fitting of the $\chi_M T$ data of **2a**, results in good agreement with the experimental data (Figure 10f). With these parameters, as in the case of **1a**, the ground spin-state of **2a** is an S = 0 state lying close to numerous excited states.

At 275 K, the $\chi_M T$ product of **6a** has a value of 39.5 cm^3 K mol^{-1} (Figure 10a) which is that expected from spin-only contributions to the magnetism, with g_{Gd} = 2.00 and g_{Ni} = 2.00. The temperature dependence of the $\chi_M T$ product indicates the presence of ferromagnetic interactions. The matrix representation of spin-Hamiltonian (2) for **6a** is of dimension 26,873,856 × 26,873,856 and cannot be diagonalised by use of standard numerical techniques. We therefore turned to the Finite Temperature Lanczos Method.[30] However, since the numerical effort is still absolutely enormous our home-written program makes use of openMP parallelisation[31] and has been executed on 40 cores of the SuperMUC Supercomputer at LRZ Garching/Germany as well as on a supercomputer at Bielefeld University. Thus, the experimental data have been interpreted by successive simulations and not by a numerical fitting routine. The obtained exchange parameters are J_{NiNi} = –24.0 cm^{-1}, J_{GdNi} = –0.34 cm^{-1} and J_{GdGd} = 0.20 cm^{-1}. The $\chi_M T$ product of **6a** is very sensitive to the magnitude of the J_{NiNi} exchange interaction, and the experimental data could also be reproduced by a parameter set involving an antiferromagnetic Ni-Ni exchange interaction J_{NiNi} = 6.0 cm^{-1}, J_{GdNi} = –1.32 cm^{-1} and J_{GdGd} = 0.20 cm^{-1}. This uncertainty could not be resolved since simplifying assumptions, such as the use of an isotropic g-factor, as described for **2a**, and omission of anisotropy terms, had to be made in order to make the numerical treatment feasible at all. Nevertheless, since the Ni-O-Ni angle is approximately 96° the exchange is most likely ferromagnetic. A single-point calculation of the VTVB data using the best-fit parameters from fitting of the $\chi_M T$ data results in good agreement with the experimental data (Figure 10g). The ground state possesses a total spin of S = 14.

Finally, the magnetic properties of compound **7a** shall be discussed. The $\chi_M T$ product of **7a** has a value of 55.9 cm^3 K mol^{-1} at 275 K (Figure 10a). We can assume that the $\chi_M T$ product at the highest temperatures is given by the paramagnetic limit, with an effective spectroscopic splitting factor for Co^{II} of g_{Co} = 2.55. Since we failed to determine the isotropic exchange parameter between Co^{II} ions in **7b**, a detailed quantitative description of the magnetic properties of **7a** is impossible. The VTVH magnetic moment data of **7a** are shown in Figure 10h. The value of the molecular magnetic moment of 46.7 μ_B at 7 T suggests a field-induced, intermediate, ground spin-state of approximately S = 20.

Magnetocalorics

We now systematically investigate the role played by the magnetic coupling and anisotropy brought by the TM^{II} ions, which can either be Zn^{II}, Cu^{II}, Ni^{II} or Co^{II}, in the magnetocaloric effect (MCE) of the complexes containing gadolinium. As representative systems, we have selected the hmp derivatives **1a**, **2a**, **6a** and **7a**.

Figure 11 shows the temperature dependence of the molar heat capacity (C/R, where R is the gas constant) for the four complexes. Below *ca.* 5 K, $C(T,B)$ depends on the applied field and is characterised by a Schottky-like behaviour, *viz.*, a relatively broad anomaly that shifts towards higher T on increasing B. Note that, in the cases of **2a** and **7a**, the field dependence of $C(T,B)$ is weak for fields up to 3 T, suggesting that these complexes are characterised by relatively strong antiferromagnetic interactions or magnetic anisotropy. The presence of sizeable, though weak, intermolecular correlations in **1a** promotes a somewhat higher height of the zero-field Schottky curve with respect to the magnetic anomalies collected with fields other than zero. At high temperatures, the non-magnetic lattice contribution dominates and can be described by the Debye model, which simplifies to the $C/R = \alpha T^3$ dependence at low T. The fits (dotted lines) provide α = 8.9×10^{-3} K^{-3} for **1a**; 9.3×10^{-3} K^{-3} for **2a**; 9.8×10^{-3} K^{-3} for **6a** and 1.0×10^{-2} K^{-3} for **7a**.

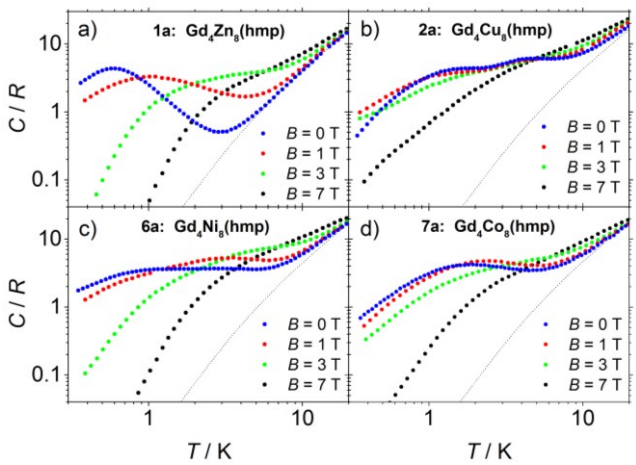

Figure 11. Heat capacity, normalized to the gas constant R, versus temperature, for several applied magnetic fields, as labelled, for **1a** (a), **2a** (b), **6a** (c) and **7a** (d). Dotted lines represent the lattice contributions.

Next, we apply $S(T,B)=\int_0^T \frac{C(T',B)}{T'}dT'$ to the experimental heat capacity in order to calculate the entropy for **1a**, **2a**, **6a** and **7a** (Figure S4). The evaluation of the magnetic entropy change, $\Delta S_m(T,\Delta B)$, is then straightforwardly obtained for a field change $\Delta B = B_f - B_i$, namely $B_i = 0$ and $B_f = 1$, 3 or 7 T (Figure 12). To facilitate the comparison between the results inferred from each complex, the $\Delta S_m(T,\Delta B)$ data are reported per molar unit and within the same ranges for the abscissa and the ordinate. Furthermore, we also calculate $\Delta S_m(T,\Delta B)$ from the experimental magnetisation data, M (Figure 10), by using the Maxwell equation:

$$\Delta S_m(T,\Delta B)=\int_{B_i}^{B_f}\left(\frac{\partial M(T,B)}{\partial T}\right)_B dB \qquad (3)$$

The magnetic entropy changes derived from the magnetisation data agree well with the corresponding results obtained independently from heat capacity data. This proves the correctness of the procedures used.

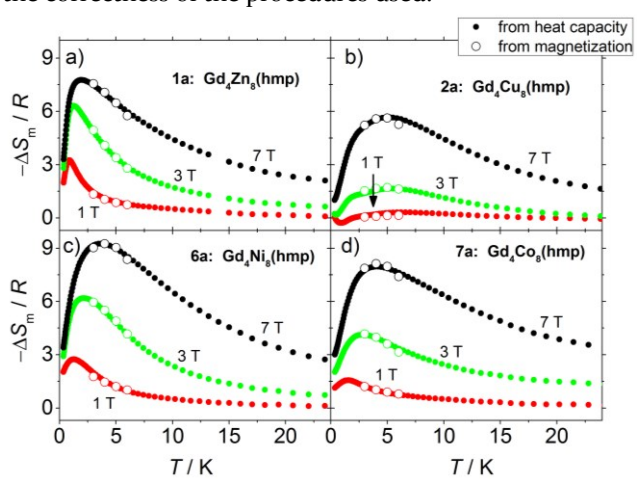

Figure 12. Magnetic entropy change (ΔS_m), normalised to the gas constant R, versus temperature for ΔB = (1 – 0) T, (3 – 0) T and (7 – 0) T, as labelled, for **1a** (a), **2a** (b), **6a** (c) and **7a** (d). The ΔS_m data are calculated using the heat capacity and magnetisation experimental data, as indicated.

Complex **1a** only has four Gd^{III} ions per molecule that contribute to the MCE. For ΔB = (7 – 0) T, $-\Delta S_m$ reaches 7.8 R, equivalent to 19.4 $Jkg^{-1}K^{-1}$ in unit mass, at T = 1.9 K. This value corresponds to a remarkably large 93% of the available entropy content, assuming four non-interacting S_{Gd} = 7/2 spins, that is, $4R\ln(2S_{Gd}+1)$ = 8.3 R. This behaviour is mainly ascribed to the very weak magnetic correlations between the Gd^{III} spins, which we have quantified to be J_{GdGd} = 0.02 cm^{-1} from fitting the magnetisation data.

By adding spins other than Gd^{III}, complexes **2a**, **6a** and **7a** have stronger magnetic interactions than in **1a**, in addition to a magnetic anisotropy in the cases of **7a** and, to lesser extent, **6a**. Therefore, relatively larger local fields set in, which, ultimately, broaden the $-\Delta S_m(T,\Delta B)$ curves and shift them towards higher temperatures,[4] as seen to occur for **2a**, **6a** and **7a**, in comparison to **1a** (Figure 12). For each complex separately, we describe the other differences that characterise the MCE of **2a**, **6a** and **7a**.

Complex **2a** has eight additional Cu^{II} spins per molecule, with respect to **1a**. This brings in additional entropy that, however, does not simply add to the $-\Delta S_m(T,\Delta B)$ curves of **1a** in our experiments. Actually, complex **2a** has a relatively low MCE with respect to **1a**. For instance, the maximum of $-\Delta S_m$ is 5.7 R = 14.6 $Jkg^{-1}K^{-1}$ at T = 5.2 K, for ΔB = (7 – 0) T. This behaviour can be understood by considering that Cu^{II} spins couple in pairs with J_{CuCu} = 11.84 cm^{-1}, as estimated from fitting the magnetisation data. It turns out that the antiferromagnetic fluctuations between Cu^{II} spins are strong against the applied fields employed. Therefore, their contribution cancels out, leaving only the Gd^{III} spins to contribute to $-\Delta S_m(T,\Delta B)$, under the experimental conditions considered. The $-\Delta S_m(T,\Delta B)$ data for **1a** (Figure 12a) and **2a** (Figure 12b) can be described using the same model based on four Gd^{III} spins per molecule, as we show in Figure S4. The only difference is the strength of the Gd-Gd coupling, which is as low as 0.02 cm^{-1} in **1a**, while **2a** has J_{GdGd} = 0.20 cm^{-1}, as estimated from the magnetisation fit. Note that, the lower the strength of the applied field, the more evident is the antiferromagnetic coupling in the MCE. For **2a** and ΔB = (1 – 0) T, for instance, $-\Delta S_m(T,\Delta B)$ becomes negative, reaching –0.3 R at T = 0.9 K. The inverse behaviour of the MCE implies an increase of T on lowering B, at certain applied field values.[32]

Complex **6a** has eight additional Ni^{II} spins per molecule, with respect to **1a**. Although complex **6a** differs from **2a** because it is characterised by predominant ferromagnetic behavior (Figure 10a), its MCE can be rationalised in the same manner as **2a**. Under our experimental conditions, each pair of Ni^{II} spins has a robust net spin state S_{NiNi} = 2, due to the aforementioned strong ferromagnetic coupling J_{NiNi} = –24.0 cm^{-1}. Each S_{NiNi} couples ferromagnetically to a Gd^{III} spin (J_{GdNi} = –0.34 cm^{-1}), thus stabilising a net spin 2 + 7/2 = 11/2, which carries the corresponding entropy content of $R\ln(2\times11/2+1)$ = 2.5 R. These spin units are antiferromagnetically coupled together within each molecule, *via* the

weakest exchange J_{GdGd} = 0.20 cm^{-1}, which involves Gd^{III} spins only. Therefore, one could reasonably expect $-\Delta S_m(T,\Delta B)$ to approach the value of 4 × 2.5 R = 10 R on increasing ΔB, provided that the strength of the applied field is not sufficient for decoupling the Ni^{II} spins from the Gd^{III} spins. Experimentally, we report $-\Delta S_m$ = 9.3 R = 23.0 Jkg^{-1}K^{-1} at T = 3.8 K, for ΔB = (7 – 0) T, consistent with our assumptions. The strong ferromagnetic interactions present in **6a** likely minimise the role that the moderate magnetic anisotropy of the Ni^{II} ions could play in the determination of the MCE for this complex.

Complex **7a** has eight additional Co^{II} spins per molecule, with respect to **1a**. The magnetothermal behavior of **7a** is determined to a large extent by the magnetic anisotropy brought in by the Co^{II} ions. Except in peculiar situations,[33] the magnetic anisotropy is a drawback in magnetic refrigeration technologies since it inhibits the attainment of large values of the MCE.[4] At sufficiently low temperatures, the spin system has access to a smaller number of states than in the absence of magnetic anisotropy. Therefore, the magnetic entropy is smaller, and so is the MCE. Not surprisingly and in spite of the additional magnetic content, the $-\Delta S_m(T,\Delta B)$ curves are significantly smaller for complex **7a** with respect to **1a**, for $\Delta B \leq 3$ T (Figure 12). Larger applied fields are likely sufficient for overcoming the anisotropy, thus permitting **7a** to attain $-\Delta S_m$ = 7.9 R = 19.7 Jkg^{-1}K^{-1} at T = 4.0 K, for ΔB = (7 – 0) T, which is comparable to **1a**.

CONCLUSIONS

Complexes of general formula $[Ln^{III}_4TM^{II}_8(OH)_8(L)_8(O_2CR)_8](X)_4$ are formed very simply and in high to moderate yields from the reaction of $Ln(NO_3)_3$ and $TM(ClO_4)_2$ and the appropriate ligand blend in a mixture of CH_2Cl_2 and MeOH in the presence of a suitable base. This family of complexes has several unusual features. It is a very rare example of a family of complexes in which almost all of the constituent parts can be changed, whilst maintaining the structural integrity of the metal core of the sample. The ability to change Ln ions is somewhat trivial, but replacing one TM^{II} ion with another is not and nor is it commonplace to observe a change in the key bridging ligand L, since this dictates the structural topology of the cage. Indeed, the whole organic sheath encasing the magnetic core can be replaced, leaving the interior untouched. This is rather remarkable. Even more unusual is that this is combined with solution stability. Detailed NMR spectroscopy of diamagnetic complex **1b** reveals the complex to be fully intact in solution and high resolution nano-ESI mass spectrometry on **2a** and **2b** show both complexes are present in two charge states with little fragmentation.

Finally, heat capacity experiments at sub-Kelvin temperatures, combined with magnetisation measurements, show that these complexes are an excellent playground for the magnetocaloric effect. We have focused on the hmp derivatives, containing gadolinium. By substitution of the non-magnetic Zn^{II} (**1a**) with Cu (**2a**), Ni (**6a**) or Co (**7a**), we were able to add to **1a** antiferromagnetic (**2a**) or ferromagnetic (**6a**) interactions or magnetic anisotropy (**7a**). This causes spins to order at higher temperatures and to affect significantly the magnetocaloric effect of these complexes. The largest (smallest) MCE is found for the ferromagnetic (antiferromagnetic) complex **6a** (**2a**). We have demonstrated that appropriate replacement of the transition metal ions allows one to tune the magnetocaloric properties of molecular coolants, and to refine the desired temperature range for possible refrigerant applications.

ASSOCIATED CONTENT

Supporting Information

Crystallographic details, additional NMR and magnetic data. This material is available free of charge *via* the Internet at http://pubs.acs.org. Data is also available at Edinburgh Datashare, http://datashare.is.ed.ac.uk/

AUTHOR INFORMATION

Corresponding Authors

E.Brechin@ed.ac.uk
evange@unizar.es
piligkos@kiku.dk

Notes

The authors declare no competing financial interest.

ACKNOWLEDGMENT

EKB thanks the EPSRC for financial support and the Velux Foundations for a Villum Visiting Professor Program grant. JS thanks the Deutsche Forschungsgemeinschaft (SCHN 615/23-1) for continuous support. Supercomputing time at the LRZ Garching (Germany) is gratefully acknowledged. GL and ME thank MINECO/FEDER (MAT2015-68204-R).

REFERENCES

(1) Spichkin, Yu. I.; Zvezdin, A. K.; Gubin, S. P.; Mischenko, A. S.; Tishin, A. M. Magnetic molecular clusters as promising materials for refrigeration in low-temperature regions. *J. Phys. D: Appl. Phys.* **2001**, *34*, 1162.

(2) (a) Debye, P. Einige bemerkungen zur magnetisierung bei tiefer temperature. *Ann. Phys.* **1926**, *386*, 1154. (*b*) Giauque, W. F. A thermodynamic treatment of certain magnetic effects. A proposed method of producing temperatures considerably below 1 absolute. *J. Am. Chem. Soc.* **1927**, *49*, 1864.

(3) (a) M. Evangelisti, F. Luis, L. J. de Jongh and M. Affronte. Magnetothermal properties of molecule-based materials. *J. Mater. Chem.* **2006**, *16*, 2534; (b) J. Schnack, R. Schmidt, J. Richter. Enhanced magnetocaloric effect in frustrated magnetic molecules with icosahedral symmetry. *Phys. Rev. B* **2007**, 76, 054413; (c) M. E. Zhitomirsky. Enhanced magnetocaloric effect in frustrated magnets. *Phys. Rev. B* **2003**, 67, 104421.

(4) Evangelisti M.; Brechin, E. K. Recipes for enhanced moleular cooling. *Dalton Trans*, **2010**, *39*, 4672.

(5) (a) Lorusso, G.; Palacios, M. A.; Nichol, G. S.; Brechin, E. K.; Roubeau, O.; Evangelisti, M. Increasing the dimensionality of cryogenic molecular coolers: Gd-based polymers and metal–organic frameworks. *Chem. Commun.* **2012**, *48*, 7592. (b) Martínez-Pérez, M.-J.; Montero, O.; Evangelisti, M.; Luis, F.; Sesé, J.; Cardona-Serra, S.; Coronado, E. Fragmenting Gadolinium: Mononuclear Polyoxometalate-Based Magnetic Coolers for Ultra-Low Temperatures. *Adv. Mater.* **2012**, *24*, 4301. (c) Guo, F.-S.; Chen, Y.-C.; Liu, J.-L.; Leng, J.-D.; Meng, Z.-S.; Vrábel, P.; Orendáč, M.; Tong, M.-L. A large cryogenic magnetocaloric effect exhibited at low field by a 3D ferromagnetically coupled Mn(II)–Gd(III)

framework material. *Chem. Commun.* **2012**, *48*, 12219. (d) Sibille, R.; Mazet, T.; Malaman, B.; François, M. A metal-organic framework as attractive magnetorefrigerant. *Chem. Eur. J.* **2012**, *18*, 12970. (e) Hooper, T. N.; Schnack, J.; Piligkos, S.; Evangelisti, M.; Brechin, E. K. The importance of being exchanged: $[Gd^{III}_4M^{II}_8(OH)_8(L)_8(O_2CR)_8]^{4+}$ clusters for magnetic refrigeration. *Angew. Chem. Int. Ed.* **2012**, *51*, 4633. (f) Birk, T.; Pedersen, K. S.; Thuesen, C. A.; Weyhermuller, T.; Schau-Magnussen, M.; Piligkos, S.; Weihe, H.; Mossin, S.; Evangelisti, M.; Bendix, J. Fluoride bridges as structure-directing motifs in 3d-4f cluster chemistry. *Inorg. Chem.* **2012**, *51*, 5435. (g) Lorusso, G.; Sharples, J. W.; Palacios, E.; Roubeau, O.; Brechin, E. K.; Sessoli, R.; Rossin, A.; Tuna, F.; McInnes, E. J. L.; Collison, D.; Evangelisti, M. A dense metal–organic framework for enhanced magnetic refrigeration. *Adv. Mater.* **2013**, *25*, 4653. (h) Langley, S. K.; Moubaraki, B.; Tomasi, C.; Evangelisti, M.; Brechin, E. K.; Murray, K. S. Synthesis, structure, and magnetism of a family of heterometallic $\{Cu_2Ln_7\}$ and $\{Cu_4Ln_{12}\}$ (Ln = Gd, Tb, and Dy) complexes: the Gd analogues exhibiting a large magnetocaloric effect. *Inorg. Chem.* **2014**, *53*, 13154. (i) Meseguer, C.; Titos-Padilla, S.; Hänninen, M.; Casas, R.; Mota, A. J.; Evangelisti, M.; Ruiz, J.; Colacio, E. Single-molecule magnet behavior and magnetocaloric effect in ferromagnetically coupled Ln^{III}-Ni^{II}-Ni^{II}-Ln^{III} (Ln^{III} = Dy^{III} and Gd^{III}) linear complexes. *Inorg. Chem.* **2014**, *53*, 12092. (j) Pedersen, K. S.; Lorusso, G.; Morales, J. J.; Weyhermüller, T.; Piligkos, S.; Singh, S. K.; Schau-Magnussen, M.; Rajaraman, G.; Evangelisti, M.; Bendix, J. Fluoride-bridged $\{Gd^{III}_3M^{III}_2\}$ (M=Cr, Fe, Ga) molecular magnetic refrigerants. *Angew. Chem. Int. Ed.* **2014**, *53*, 2394. (k) Abellán, G.; Mínguez Espallargas, G.; Lorusso, G., Evangelisti, M., Coronado, E. Layered gadolinium hydroxides for low-temperature magnetic cooling. *Chem. Commun.* **2015**, *51*, 14207. (l) Sethi, W.; Sanz, S.; Pedersen, K. S.; Sørensen, M. A.; Nichol, G. S.; Lorusso, G.; Evangelisti, M.; Brechin, E. K.; Piligkos, S. Magnetic and magnetocaloric properties of an unusual family of carbonate-panelled $[Ln^{III}_6Zn^{II}_2]$ cages. *Dalton Trans.* **2015**, *44*, 10315. (m) Rajeshkumar, T.; Annadata, H. V.; Evangelisti, M.; Langley, S. K.; Chilton, N. F.; Murray, K. S.; Rajaraman, G. Theoretical studies on polynuclear $\{Cu^{II}_5Gd^{III}_n\}$ clusters (n = 4, 2): towards understanding their large magnetocaloric effect. *Inorg. Chem.* **2015**, *54*, 1661.

(6) Affronte, M.; Ghirri, A.; Carretta, S.; Amoretti, G.; Piligkos, S.; Timco, G. A.; Winpenny, R. E. P. Engineering molecular rings for magnetocaloric effect. *Appl. Phys. Lett.* **2004**, *84*, 3468.

(7) (a) Evangelisti, M.; Candini, A.; Ghirri, A.; Affronte, M.; Brechin, E. K.; McInnes, E. J. L. Spin-enhanced magnetocaloric effect in molecular nanomagnets. *Appl. Phys. Lett.* **2005**, *87*, 072504. (b) Shaw, R.; Laye, R. H.; Jones, L. F.; Low, D. M.; Talbot-Eeckelaers, C.; Wei, Q.; Milios, C. J.; Teat, S.; Helliwell, M.; Raftery, J.; Evangelisti, M.; Affronte, M.; Collison, D.; Brechin, E. K.; McInnes, E. J. L. 1,2,3-triazolate-bridged tetradecametallic transition metal clusters $[M_{14}(L)_6O_6(OMe)_{18}X_6]$ (M = Fe^{III}, Cr^{III} and $V^{III/IV}$) and related compounds: ground-state spins ranging from S = 0 to S = 25 and spin-enhanced magnetocaloric effect. *Inorg. Chem.* **2007**, *46*, 4968.

(8) Manoli, M.; Johnstone, R. D. L.; Parsons, S.; Murrie, M.; Affronte, M.; Evangelisti, M.; Brechin, E. K. A ferromagnetic mixed-valent Mn supertetrahedron: towards low-temperature magnetic refrigeration with molecular clusters. *Angew. Chem. Int. Ed.* **2007**, *46*, 4456.

(9) Manoli, M.; Collins, A.; Parsons, S.; Candini, A.; Evangelisti, M.; Brechin, E. K. Mixed-valent Mn supertetrahedra and planar discs as enhanced magnetic coolers. *J. Am. Chem. Soc.* **2008**, *130*, 11129.

(10) Sedlakova, L.; Hanko, J.; Orendacova, A.; Orendáč, M.; Zhou, C. L.; Zhu, W. H.; Wang, B. W.; Wang, Z. M.; Gao, S. Magnetism and magnetocaloric effect in S = 7/2 Heisenberg antiferromagnet $Gd_2(fum)_3(H_2O)_4{\cdot}3H_2O$. *J. Alloy. Compd.* **2009**, *487*, 425.

(11) Karotsis, G.; Evangelisti, M.; Dalgarno, S. J.; Brechin, E. K. A Calix[4]arene 3d/4f Magnetic Cooler. *Angew. Chem. Int. Ed.* **2009**, *48*, 9928.

(12) (a) Sessoli, R. Chilling with Magnetic Molecules. *Angew. Chem. Int. Ed.* **2012**, *51*, 43. (b) Sharples, J. W.; Collison, D. Coordination compounds and the magnetocaloric effect. *Polyhedron*, **2013**, *54*, 91. (c) Zheng, Y. Z.; Zhou, G. J.; Zheng, Z. P.; Winpenny, R. E. P. *Chem. Soc. Rev.* **2014**, *43*, 1462.

(13) See for example (a) Bencini, A.; Benelli, C.; Caneschi, A.; Carlin, R. L.; Dei, A.; Gatteschi, D. Crystal and molecular structure of and magnetic coupling in two complexes containing gadolinium(III) and copper(II) ions. *J. Am. Chem. Soc.* **1985**, *107*, 8128. (b) Andruh, M.; Ramade, I.; Codjovi, E.; Guillou, O.; Kahn, O.; Trombe, J. C. Crystal structure and magnetic properties of $[Ln_2Cu_4]$ hexanuclear clusters (where Ln = trivalent lanthanide). Mechanism of the gadolinium(III)-copper(II) magnetic interaction. *J. Am. Chem. Soc.* **1993**, *115*, 1822, (c) Costes, J. P.; Dahan, F.; Dupuis, A.; Laurent, J. P. A general route to strictly dinuclear Cu(II)/Ln(III) complexes. Structural determination and magnetic behavior of two Cu(II)/Gd(III) complexes. *Inorg. Chem.* **1997**, *36*, 3429. (d) Benelli, C.; Gatteschi, D. Magnetism of lanthanides in molecular materials with transition-metal ions and organic radicals. *Chem. Rev.* **2002**, *102*, 2369.

(14) Langley, S. K.; Chilton, N. F.; Moubaraki, B.; Hooper, T.; Brechin, E. K.; Evangelisti, M.; Murray, K. S. Molecular coolers: the case for $[Cu^{II}_5Gd^{III}_4]$. *Chem. Sci.* **2011**, *2*, 1166.

(15) The pro-ligands Hhmp and H_2pdm have been extensively employed by Christou and co-workers, particularly in 3*d* cluster chemistry. See for example: (a) Bolcar, M. A.; Aubin, S. M. J.; Folting, K.; Hendrickson, D. N.; Christou, G. A new manganese cluster topology capable of yielding high-spin species: mixed-valence $[Mn_7(OH)_3Cl_3(hmp)_9]^{2+}$ with S ≥ 10. *J. Chem. Soc. Chem. Commun.* **1997**, 1485. (b) Boskovic, C. Brechin, E. K.; Streib, W. E.; Folting, K.; Hendrickson, D. N.; Christou, G. A new class of single-molecule magnets: mixed-valent $[Mn_{12}O_8Cl_4(O_2CPh)_8(hmp)_6]$. *Chem. Commun.* **2001**, 467. (c) Murugesu, M.; Mishra, A.; Wernsdorfer, W.; Abboud, K. A.; Christou, G. Mixed 3d/4d and 3d/4f metal clusters: tetranuclear $Fe_2^{III}M_2^{III}$ (MIII = Ln, Y) and $Mn_2^{IV}M_2^{III}$ (M = Yb, Y) complexes, and the first Fe/4f single-molecule magnets. *Polyhedron*, **2006**, *25*, 613. (d) Yoo, J.; Brechin, E. K.; Yamaguchi, A.; Nakano, M.; Huffman, J. C.; Maniero, A. L.; Brunel, L. C.; Awaga, K.; Ishimoto, H.; Christou, G.; Hendrickson, D. N. Single-molecule magnets: a new class of tetranuclear manganese magnets. *Inorg. Chem.* **2000**, *39*, 3615.

(16) Barran, P. E.; Shirran, S. L. The use of ESI-MS to probe the binding of divalent cations to calmodulin. *J. Am. Soc. Mass Spectrom.* **2009**, *20*, 1159.

(17) Barran, P. E.; Cole, H. L.; Kalapothakis, J. M. D.; Bennett, G.; MacPhee, C. E. Characterizing early aggregates formed by an amyloidogenic peptide by mass spectrometry. *Angew. Chem. Int. Ed.* **2010**, *49*, 9448.

(18) Ujma, J.; De Cecco, M.; Chepelin, O.; Levene, H.; Moffat, C.; Pike, S. J.; Lusby, P. J.; Barran, P. E. Shapes of supramolecular cages by ion mobility mass spectrometry. *Chem. Commun.* **2012**, *48*, 4423.

(19) Corradini, V.; Ghirri, A.; Candini, A.; Biagi, R.; del Pennino, U.; De Renzi, V.; Dotti, G.; Otero, E.; Hooper, T. N.; Inglis, R.; Brechin, E. K.; Affronte, M. Surface Investigation on Gd_4M_8 (M = Zn, Ni) single molecule coolers. *Adv. Func. Mater.* **2014**, 24, 4782.

(20) Iasco, O.; Novitchi, G.; Jeanneau, E.; Wernsdorfer, W.; Luneau, D. Benzoxazole-based heterometallic dodecanuclear complex $[Dy^{III}_4Cu^{II}_8]$ with single-molecule-magnet behavior. *Inorg. Chem.* **2011**, *50*, 7373.

(21) Aronica, C.; Pilet, G.; Chastanet, G.; Wernsdorfer, W.; Jacquot, J. F.; Luneau, D. A nonanuclear dysprosium(III)–copper(II) complex exhibiting single-molecule magnet behavior

with very slow zero-field relaxation. *Angew. Chem. Int. Ed.* **2006**, *45*, 4659.

(22) Karotsis, G.; Kennedy, S.; Teat, S. J.; Beavers, C. M.; Fowler, D. A.; Morales, J. J.; Evangelisti, M.; Dalgarno, S. J.; Brechin, E. K. [$Mn^{III}_4Ln^{III}_4$] calix[4]arene clusters as enhanced magnetic coolers and molecular magnets. *J. Am. Chem. Soc.* **2010**, *132*, 12983.

(23) Mereacre, V.; Akhtar, M. N.; Lan, Y. H.; Ako, A. M.; Clérac, R.; Anson, C. E.; Powell, A. K. Structures and magnetic properties of $Mn^{III}_4Ln^{III}_4$ aggregates with a "square-in-square" topology. *Dalton Trans.* **2010**, *39*, 4918.

(24) Zheng, Y. Z.; Evangelisti, M.; Winpenny, R. E. P. Co–Gd phosphonate complexes as magnetic refrigerants. *Chem. Sci.* **2011**, *2*, 99.

(25) Van, Q. N.; Smith, E. M.; Shaka, A. J. Observation of long-range small-molecule NOEs using a neoteric sensitivity enhancement scheme. *J. Mag. Reson*. **1999**, *141*, 191.

(26) Robinson, P. T.; Pham, T. N.; Uhrín, D. In phase selective excitation of overlapping multiplets by gradient-enhanced chemical shift selective filters. *J. Magn. Reson*. **2004**, *170*, 97.

(27) Thrippleton, M. J.; Keeler, J. Elimination of Zero-Quantum Interference in Two-Dimensional NMR Spectra. *Angew. Chem. Int. Ed.* **2003**, *42*, 3938.

(28) Press, W. H.; Teukolsky, S. A.; Vetterling, W. T.; Flannery, B. P. Numerical Recipes in C: The Art of Scientific Computing, Cambridge University Press, Cambridge, 2nd Ed, **1992**.

(29) Bencini, A.; Gatteschi, D. Electron Paramagnetic Resonance of Exchange Coupled Clusters, Springer, Berlin, **1990**.

(30) (a) Jaklič, J.; Prelovsěk, P. Lanczos method for the calculation of finite-temperature quantities in correlated systems. *Phys. Rev. B.* **1994**, *49*, 5065; (b) Schnack, J.; Wendland, O. Properties of highly frustrated magnetic molecules studied by the finite-temperature Lanczos method. *Eur. Phys. J. B*. **2010**, *78*, 535; (c) Schnack, J.; Heesing, C. Application of the finite-temperature Lanczos method for the evaluation of magnetocaloric properties of large magnetic molecules. *Eur. Phys. J. B*. **2013**, *86*, 46.

(31) Schnack, J.; Hage, P.; Schmidt, H.-J. Efficient implementation of the Lanczos method for magnetic systems. *J. Comput. Phys*. **2008**, 227, 4512.

(32) Sharples, J. W.; Collison, D.; McInnes, E. J. L.; Schnack, J.; Palacios, E.; Evangelisti, M. Quantum signatures of a molecular nanomagnet in direct magnetocaloric measurements. *Nat. Commun*. **2014**, 5, 5321.

(33) Lorusso, G.; Roubeau, O.; Evangelisti, M. Rotating magnetocaloric effect in an anisotropic molecular dimer *Angew. Chem. Int. Ed.* **2016**, *55*, 3360.

SYNOPSIS TOC (Word Style "SN_Synopsis_TOC"). A family of $[Ln^{III}_4TM^{II}_8]$ complexes, in which all the constituent parts can be interchanged while maintaining structural integrity, allows for a detailed examination of contributions to the magnetocaloric effect.

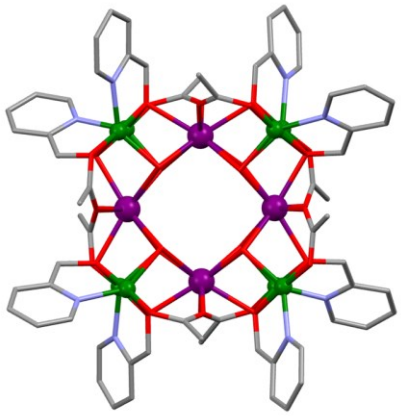

Insert Table of Contents artwork here